Dynamics Study of the H + ArO_2 Multichannel Reaction

J. M. C. Marques, W. Wang, A. A. C. C. Pais, and A. J. C. Varandas*

Departamento de Química, Universidade de Coimbra, P-3049 Coimbra Codex, Portugal

Received: June 21, 1996; In Final Form: August 23, 1996[⊗]

Trajectory calculations have been carried out for the title reaction over the range of translational energies $0.25 \leq E_{tr}/\text{kcal mol}^{-1} \leq 131.4$. We present reactive cross sections for formation of stable HO_2 for translational energies up to 8.0 kcal mol^{-1}, while for O_2 formation the reported cross sections extend over the whole range of translational energies. The former cross sections are shown to decrease with increasing translational energy, while the latter cross sections show a slight increase leading to a broad maximum and finally approach zero at high energies. Similarly, the formation of OH products has been investigated in detail and compared with the corresponding process in the absence of argon. Formation and dissociation of energized HO_2* complexes have also been analyzed and the decay rates rationalized by means of a simple two-step kinetic mechanism.

1. Introduction

The three-body gas-phase reaction

$$H + O_2 + M \rightarrow HO_2 + M \quad (1)$$

where M is usually a rare gas, plays an important role in atmospheric HO_2 formation and combustion processes. This recombination reaction of atomic hydrogen with molecular oxygen is the dominant loss mechanism for H atoms in both the troposphere and stratosphere and acts as the chain termination step at the explosion limit of the hydrogen−oxygen system. Although the corresponding thermal rate coefficient has been the subject of many[1−6] experimental measurements, only a few studies have suggested its theoretical interpretation in terms of elementary steps. Regarding the high-temperature rate coefficient measurements, most studies have been obtained from shock tube or flame data using argon as the third body.[7−11] At 300 K, the available kinetic studies for the title reaction consist of scattered experiments using both direct[12−18] and indirect (see ref 3 and references therein) techniques. More recently, Carleton *et al.*[2] have carried out studies using several third bodies, which include N_2 at 298 −580 K, H_2O at 575−750 K, and Ar at 298 K.

Theoretically, Galluci and Schatz[19] have employed the classical trajectory method to study the He + HO_2* system (the star indicates HO_2 molecules excited above the dissociation threshold) and reported cross sections for energy transfer, stabilization, and dissociation of HO_2*. In addition, Brown and Miller[20] have carried out calculations for the same system, with the HO_2* complexes being excited to energies just above the dissociation threshold. Both studies[19,20] have used the Melius−Blint[21] potential energy surface for the HO_2 radical. In a similar context, Gelb[22] has performed calculations for the Ar−O_3 system, employing the O_3 potential energy function of Varandas and Murrell.[23]

In a recent Letter,[24] the authors have obtained the termolecular rate coefficient for the three-body recombination processes H + O_2 + Ar → HO_2 + Ar and O + O_2 + Ar → O_3 + Ar using the two-step chaperon mechanism

$$Ar + O_2 \rightleftharpoons ArO_2 \quad (2)$$

$$X + ArO_2 \rightarrow XO_2 + Ar \quad (3)$$

where X stands for a hydrogen or oxygen atom, respectively. The first step is a fast complex formation equilibrium, in contrast with the second which is the rate-determining process. The results concerning the termolecular rate coefficients for HO_2 formation have shown good agreement with the experimental measurements.[1,2,5] In turn, the results for ozone formation have indicated fair agreement with experimental results while showing some improvement over previous theoretical calculations,[25] which have employed the energy-transfer mechanism[26−28] and fits to *ab initio* energies[29,30] using the many-body expansion[31] method. Although competitive, it is impossible to say which mechanism predominates, and probably they should both be considered.

The identification of HO_2 product molecules arising from the title reaction is not free from some ambiguity, especially if based simply on geometrical criteria. Since not all the initial translational energy is transferred to the receding Ar atom, the H + ArO_2 collisions may lead to formation of energized HO_2* complexes. This can easily be tested by comparing the total internal energy of the formed hydroperoxyl radical with the corresponding energy threshold for H + O_2 dissociation. Thus, it will be interesting to examine the detailed mechanism for the unimolecular dissociation reaction

$$HO_2^* \rightarrow H + O_2 \quad (4)$$

which has been a topic of recent theoretical investigations[32−34] using the DMBE IV[35] potential energy surface for the ground electronic state of the hydroperoxyl radical (for improvements on the DMBE IV surface, see ref 36). Song *et al.*[32] have also utilized quantum and semiclassical variational transition state models to obtain microcanonical rate constants for reaction 4, and a comparison of the different results allowed them to conclude that there is weak coupling between the O−O stretch and H−O_2 bend modes along the reaction path. Moreover, Dobbyn *et al.*[33] have reported the bound states of HO_2 up to the dissociation threshold. They observed that although the wave functions are mostly irregular close to the dissociation threshold, there are some regular states that are associated with large excitation in the O_2 stretching mode and little excitation in the other vibrational coordinates. Based on these results, Dobbyn *et al.*[33] have suggested the existence of regions of regularity (again, probably due to a partial decoupling of the O−O stretching coordinate from the other two modes) in the classical phase space, which have been associated with "vague tori".[37] These have been suggested[38] to provide bottlenecks to

[⊗] Abstract published in *Advance ACS Abstracts,* October 1, 1996.

S0022-3654(96)01863-1 CCC: $12.00

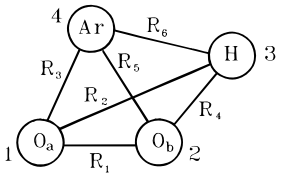

Figure 1. Schematic representation of the system of coordinates used in the present work. For clarity, the oxygen atoms are labeled O_a and O_b.

the intramolecular vibrational energy redistribution and associated with approximate constants of motion that confine trajectories to quasiperiodic orbits even in seemingly chaotic regions of phase space. In addition, a paper has appeared in the literature by Mandelshtam *et al.*[34] reporting vibrational energies and resonances for nonrotating HO_2; both studies have shown consistent results. More recently, Dai and Zhang[39] calculated numerous bound and resonance (both inelastic and reactive) states for HO_2 using a time-dependent wave packet approach and the DMBE IV potential energy surface.

In this work, we report a dynamics study of the title reaction over the range of translational energies $0.25 \leq E_{tr}/\text{kcal mol}^{-1} \leq 131.4$. Besides the main dynamical aspects of the H + ArO_2 reactive system, we give emphasis to the argon solvation effects in the cross section for OH formation and to the study of HO_2* dissociation. The plan of the paper is as follows. In section 2, we describe the potential energy surface for $ArHO_2$. All computational procedures are reported in section 3. Section 4 discusses the details of the H + ArO_2 reaction dynamics. The cross sections for HO_2, O_2, and OH formation are presented in section 5, while section 6 analyzes the dissociation of the HO_2* complexes. The conclusions are in section 7.

2. Potential Energy Surface for $ArHO_2$

Since the main details concerning the $ArHO_2$ potential energy surface have been discussed elsewhere,[24,35] we present here only some additional features with importance for the dynamics of the title reaction. In terms of the six internuclear distances shown in Figure 1, the $ArHO_2$ potential energy surface assumes the form

$$V_{ArHO_2}(\mathbf{R}) = V_{HO_2}(R_1,R_2,R_4) + V_{ArO}(R_3) + V_{ArO}(R_5) + V_{ArH}(R_6) \quad (5)$$

where $\mathbf{R} \equiv (R_1, ..., R_6)$, V_{HO_2} is the DMBE IV[35] potential for the hydroperoxyl radical, and the pair-potentials[24] V_{ArO} and V_{ArH} describe the ArO and ArH interactions, respectively. To represent the pair-potentials, we have employed the EHFACE2 model,[40] which have been calibrated[24] to reproduce the attributes (well depth ϵ_m and location R_m) of the corresponding experimental minima: $\epsilon_m = -2.798 \times 10^{-4} E_h$ at $R_m = 6.65\ a_0$ for ArO[41] and $\epsilon_m = -1.5273 \times 10^{-4} E_h$ at $R_m = 6.84\ a_0$ for ArH.[42]

Figure 2 shows a contour plot for the hydrogen atom moving coplanarly around the ArO_2 molecule fixed in its equilibrium geometry; the solid dot represents the center-of-mass of the triatomic molecule. We note the absence of energy barrier for the H atom to approach the reactant ArO_2 molecule from the side opposite to the Ar atom. Indeed, this almost inhibits reaction for the corresponding angles of attach. Also depicted in Figure 2 are the potential barriers next to the O atoms and the saddle point for isomerization. Note that the center-of-mass of the reactant molecule falls in the repulsive region close to the Ar atom, and hence, zero-impact parameter trajectories represent nearly head-on collisions with argon.

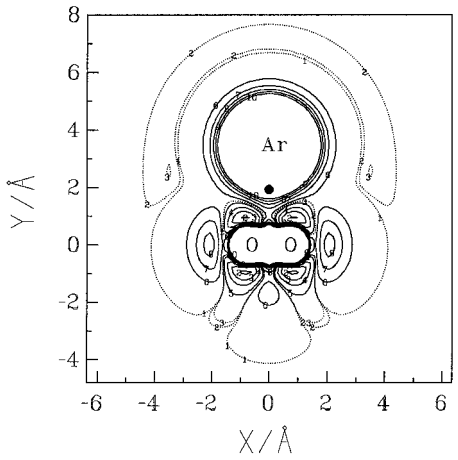

Figure 2. Isoenergy contour plot for the H atom moving around an ArO_2 molecule fixed at its equilibrium geometry. The solid dot indicates the ArO_2 center-of-mass.

3. Computational Procedures

3.1. Classical Trajectory Method. The quasiclassical trajectory method as applied to atom + triatom collisions[43,44] has been used in the present work to study the H + ArO_2 reaction. According to this method,[43−47] the cross sections are obtained from

$$\sigma_i(E_{tr}) = g\pi b_{max}^2 N_i(E_{tr})/N \quad (6)$$

where i labels the reactive channel and the factor $g = 1/3$ is the same as for $H(^2S) + O_2(^3\Sigma_g^-)$ reaction.[48−52] The remaining symbols in eq 6 have their usual meaning, *e.g.*, N_i is the number of reactive trajectories on the ith channel out of a total of N trajectories considered for the statistical analysis. Similarly, the 68% confidence intervals are given by

$$\Delta\sigma_i = \sigma_i(E_{tr})\left[\frac{N - N_i(E_{tr})}{NN_i(E_{tr})}\right]^{1/2} \quad (7)$$

with N_i, σ_i, and $\Delta\sigma_i$ depending on the initial translational energy (E_{tr}) of the approaching reactants. Although the total number of trajectories, N, may also be chosen to depend on E_{tr}, this dependence is clearly arbitrary, and hence, it is not explicitly stated in the aforementioned formulas.

In the remainder of this subsection, we address the way the reactants have been prepared. Usually, the initial vibrational states of the triatomic are defined in terms of the corresponding normal mode frequencies, and the initial rotational energy is set by employing the rigid rotor approximation. However, as it is well established,[50,53,54] the quasiclassical trajectory method suffers from the problem of zero-point energy leak. Because of this, and since rotational−vibrational energy conversion is possible, we have fixed initially the triatomic molecule at its equilibrium geometry to integrate the classical equations of motion. This scheme avoids unphysical energy flow from the bound modes to unbound ones, which would otherwise be responsible for an early breakoff of Ar−O bonds even before any significant interaction with the H atom has occurred.

3.2. Identification of the Reactive Channels. Atom−triatom collisions can lead to 14 possible channels, 2 of which correspond to the nonreactive and completely dissociative processes, respectively. As before,[24] we do not consider as distinct channels the various isomers of a given species. Thus, a possible scheme for identification of the various reactive channels requires the inspection of every interatomic distance that becomes increasingly large and the simultaneous charac-

TABLE 1: Definition of the 14 Channels in the H + ArO_2 Collisions[a]

channel	products	R_1/Å	R_2/Å	R_3/Å	R_4/Å	R_5/Å	R_6/Å
1	H + ArO_2	1.21	∞	3.52	∞	3.52	∞
		<1.66	>20.0	<4.40	>20.0	<4.40	>20.0
2	Ar + HO_2	1.33	0.97	∞	1.83	∞	∞
		<1.66	<2.29	>4.68	<2.29	>4.68	>4.68
3	O_a + ArO_bH	∞	∞	∞	0.97	3.52	3.62
		>5.63	>5.63	>5.63	<2.29	<4.40	<4.52
4	O_b + ArO_aH	∞	0.97	3.52	∞	∞	3.62
		>5.63	<2.29	<4.40	>5.63	>5.63	<4.52
5	Ar + H + O_2	1.21	∞	∞	∞	∞	∞
		<1.66	>4.70	>4.70	>4.70	>4.70	>4.70
6	Ar + O_a + O_bH	∞	∞	∞	0.97	∞	∞
		>5.51	>5.51	>5.51	<2.29	>5.51	>5.51
7	Ar + O_b + O_aH	∞	0.97	∞	∞	∞	∞
		>5.51	<2.29	>5.51	>5.51	>5.51	>5.51
8	O_a + H + ArO_b	∞	∞	∞	∞	3.52	∞
		>5.51	>5.51	>5.51	>5.51	<4.40	>5.51
9	O_b + H + ArO_a	∞	∞	3.52	∞	∞	∞
		>5.51	>5.51	<4.40	>5.51	>5.51	>5.51
10	O_a + O_b + ArH	∞	∞	∞	∞	∞	3.62
		>4.70	>4.70	>4.70	>4.70	>4.70	<4.52
11	O_2 + ArH	1.21	∞	∞	∞	∞	3.62
		<1.66	>4.70	>4.70	>4.70	>4.70	<4.52
12	O_aH + ArO_b	∞	0.97	∞	∞	3.52	∞
		>5.51	<2.29	>5.51	>5.51	<4.40	>5.51
13	O_bH + ArO_a	∞	∞	3.52	0.97	∞	∞
		>5.51	>5.51	<4.40	<2.29	>5.51	>5.51
14	O_b + O_a + H + Ar	∞	∞	∞	∞	∞	∞
		>5.63	>5.63	>5.63	>5.63	>5.63	>5.63

[a] The second entry defines the various channels, which are specified in the first entry; see text.

terization of the product molecules on geometric grounds. Accordingly, we define the 14 channels for the collisional system H + ArO_2 as shown in the first entries of Table 1. Clearly, the characterization of the product molecules can be done by comparing at every point along the trajectory the interatomic distances R_i (i = 1, ..., 6) with the corresponding equilibrium values there reported. However, to avoid any ambiguity (since it is not possible to know *a priori* which products will be formed at the end of the trajectory), all interatomic distances must be compared at each step with the corresponding bond distances in equilibrium $ArHO_2$. In the case of indistinguishable fragments, such as O_a−H and O_b−H (*a* and *b* are arbitrary labels of the oxygen atoms), we choose as the reference the largest equilibrium bond distance. Of course, all reference bond distances must additionally admit a small tolerance (typically 25%) to acount for the vibrational motion of the formed molecules. Thus, these will be considered as formed when the corresponding interatomic distances satisfy the requirements indicated in the second entries of Table 1.

It remains to specify the distances $R_M^{(i)}$ (i = 1−14), beyond which it is reasonable to consider the products as separated. For simplicity, we have adopted in this scheme only one $R_M^{(i)}$ distance per channel. Thus, $R_M^{(i)}$ is associated with the *i*-type products and must replace for practical purposes the infinities indicated in the first entries of Table 1. Because the velocity of the receding products depends on their reduced mass, the $R_M^{(i)}$ values must also account for the specific mass factor. This is achieved through the relation[24]

$$\frac{R_M^{(i)}}{R_M^{(j)}} = \left[\frac{\mu^{(j)}}{\mu^{(i)}}\right]^{1/2} \tag{8}$$

from which one may generate the remaining $R_M^{(j)}$ distances once it is fixed for the *i*th-channel; $\mu^{(i)}$ and $\mu^{(j)}$ stand for the reduced masses of the products in channels *i* and *j*, respectively.

TABLE 2: Summary of the Trajectory Calculations for the H + ArO_2 Reaction over the Range of Translational Energies 0.25 ≤ E_{tr}/kcal mol^{-1} ≤ 8.0[b]

E_{tr}/kcal mol^{-1}	b_{max}/Å	N_{inc}	N	N_1	N_2	N_2*	N_5
0.25	5.75	8	1492	1303	187	2	
0.50	5.25	2	1498	1302	100	95	1
1.0	4.75	1	1499	1282	40	155	22
2.0	4.5		1500	1282	10	157	51
4.0	4.0		1500	1251	2	152	95[a]
8.0	4.0		1500	1266	1	118	115

[a] This includes one trajectory which led to O_2 +ArH (channel 11). [b] See text.

According to eq 8, a small reduced mass implies a large value for $R_M^{(i)}$ and *vice versa*. It has been shown[24] that the reduced mass comprises a wide range of values, varying from $\mu^{(1)}$ = 0.99 to $\mu^{(2)}$ = 18.07. Thus, by arbitrarily fixing $R_M^{(1)}$ = 20 Å, one obtains the values for $R_M^{(j)}$ (j = 2, ..., 14). These are also given in the second entries of Table 1. Although arbitrary, our choice of $R_M^{(1)}$ results from an attempt to account for the relatively small reduced mass of channel 1 while avoiding long integration times.

3.3. Technical Specifications. All trajectories have been run using an extensively adapted version[24] of the MERCURY[55] program. The determination of the step size for numerical integration has been done by trial and error on the basis of accuracy requirements. The value 1.2 × 10^{-16} s has been found to be sufficient to warrant conservation of energy to better than 10^{-3} kcal mol^{-1}.

Batches of 1500 trajectories have then been run for E_{tr} = 0.25, 0.50, 1.0, 2.0, 4.0, and 8.0 kcal mol^{-1}, keeping the ArO_2 molecule initially fixed at the corresponding equilibrium geometry. To select the maximum value of the impact parameter for which there is reaction, b_{max}, we followed the usual procedure by computing batches of 100 trajectories for fixed values of *b*. Although optimized for the Ar + HO_2 outcome, the b_{max} values so obtained have been found to be also good for studying the formation of O_2. They have been calculated with an accuracy of ±0.25 Å and are reported for each translation energy in Table 2. Also shown in this table is the number of incomplete trajectories (N_{inc}) that lasted longer than the time limit initially allowed for the integration procedure, *i.e.*, 9.6 × 10^{-12} s. Because such trajectories cannot be assigned to 1 of the 14 channels, they have been removed from the total number of trajectories (N) for the purpose of statistical analysis. The results, shown in Table 2, are discussed in sections 4 and 5.

For the range of translational energies 15.5 ≤ E_{tr}/kcal mol^{-1} ≤ 131.4, the batch size has been increased to 3000 trajectories to warrant better converged cross sections. In such cases, b_{max} has been optimized for the reactive channels leading to OH or ArOH (see Table 1). The calculated values are given in Table 3.

4. Dynamical Details of H + ArO_2 Reaction

4.1. Energetics and Illustrative Trajectories. Although 14 distinct outcomes are possible for the collision between a hydrogen atom and the ArO_2 van der Waals molecule, only a few of them are likely to occur at low energies. Indeed, it is seen from Figure 3 that only three product channels are opened for the range of translational energies 0.25 ≤ E_{tr}/kcal mol^{-1} ≤ 8.0. They correspond to formation of Ar + HO_2 (channel 2), which has an exoergicity of −54.51 kcal mol^{-1}, and O_2 + ArH (channel 11) and Ar + H + O_2 (channel 5), which have endoergicities of 0.26 and 0.35 kcal mol^{-1}, respectively. Of

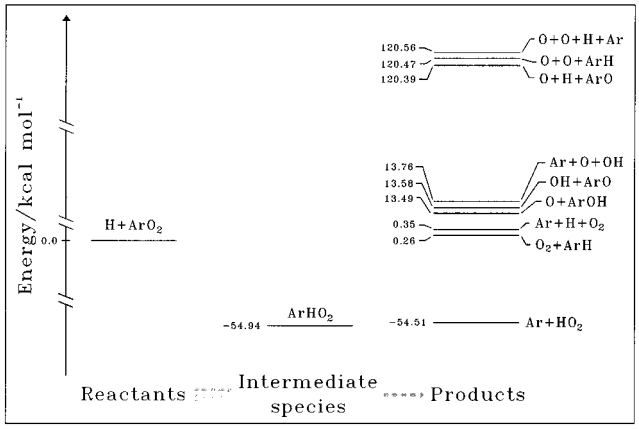

Figure 3. Energetic features of the H + ArO_2 reaction. Note that the zero of energy corresponds to the reactants and that all other channels are referred to this one.

TABLE 3: Summary of the Trajectory Calculations for the H + ArO_2 Reaction over the Range of Translational Energies 15.5 ≤ E_{tr}/kcal mol^{-1} ≤ 131.4[b]

E_{tr}/kcal mol^{-1}	b_{max}/Å	N_2*	N_3	N_4	N_6	N_7	N_{12}	N_{13}	N^{OH}	σ_r^{OH}/Å^2
15.5	4.0	156	1	0	0	0	0	1	2	0.011 ± 0.008
19.1	4.0	123	0	0	1	2	2	0	5	0.028 ± 0.012
27.6	3.5	63	0	1	5	7	3	4	20	0.086 ± 0.019
42.8	3.5	20	4	1	16	13	12	4	50	0.214 ± 0.030
59.3	3.5	13	3	6	10	15	5	5	44	0.188 ± 0.028
71.7	3.0	8	8	2	23	16	9	9	67	0.210 ± 0.025
95.6	2.75	6	3	3	27	25	17	14	89	0.235 ± 0.024
107.6	2.75	5	10	2	23	16	9	10	70	0.185 ± 0.022
119.5	2.75	1	6	0	17	11	7	1	42	0.111 ± 0.017
131.4[a]	2.75	1	2	0	10	10	2	5	29	0.076 ± 0.014

[a] For this translational energy, there have been three dissociative trajectories. The corresponding cross section is 0.008 ± 0.004 Å^2. [b] For all translational energies, the number of integrated trajectories has been 3000. Note that in column 10, $N^{OH} = \sum_{i \neq 2} N_i$. See text.

course, there is always the possibility of reforming the H + ArO_2 reactants, as indicated by the double arrow in Figure 3. In turn, with the reactant molecule fixed at its equilibrium geometry, the channels leading to Ar + O + OH, OH + ArO, and O + ArOH are opened only for translational energies above 13.49 kcal mol^{-1}. This is the case for the high-energy regime discussed in section 5.2. Moreover, channels number 8, 9, 10, and 14 are opened only for translational energies above 120 kcal mol^{-1}.

Tables 2 and 3 show the trajectory results for the H + ArO_2 reaction. In Table 2, we distinguish between stable HO_2 molecules (N_2) and those that have an internal energy exceeding the H + O_2 limit (N_2*). All trajectories of both sets have been identified using the geometrical criteria described in section 3.2, the assignment to N_2 or N_2* being done *a posteriori* by comparing the internal energy of HO_2/HO_2* against the value of 54.86 kcal mol^{-1} associated with the H + O_2 dissociation limit (see Figure 3). We should note that the HO_2* complexes with internal energy above ~68 kcal mol^{-1} can also dissociate, though not frequently, to form O + OH. For the range 15.5 ≤ E_{tr}/kcal mol^{-1} ≤ 131.4, no stable HO_2* complexes are formed (see Table 3).

Figure 4 shows the interatomic distance vs time plot for a typical trajectory leading to a stable HO_2 molecule, while Figure 5 illustrates another for the formation of an energized HO_2* species. In the latter figure, after the HO_2* has been formed [part a of Figure 5], we have allowed the trajectory to continue until dissociation into H + O_2 [part b] has occurred. We note that the time elapsed from the beginning of the trajectory to formation of HO_2* is only a small fraction of the total integration

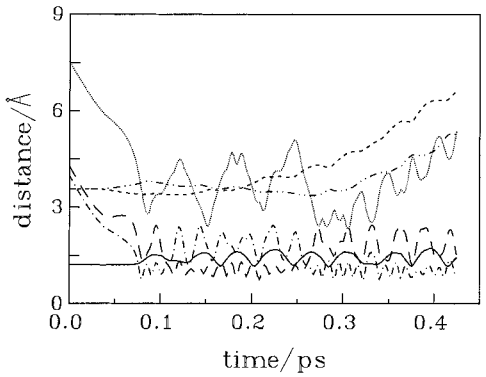

Figure 4. Distance vs time plot for a typical trajectory leading to a stable HO_2 product: (—) R_1; (— — —) R_2; (- - -) R_3; (-·-) R_4; (-···) R_5; (···) R_6. The initial translational energy is 4.0 kcal mol^{-1}. The time is given in picoseconds.

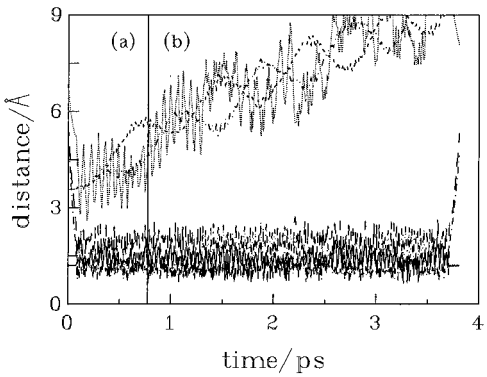

Figure 5. As in Figure 4 but for a trajectory leading to an energized HO_2* molecule [part a]. The trajectory is allowed to continue until dissociation into H + O_2 occurs [part b]. See text.

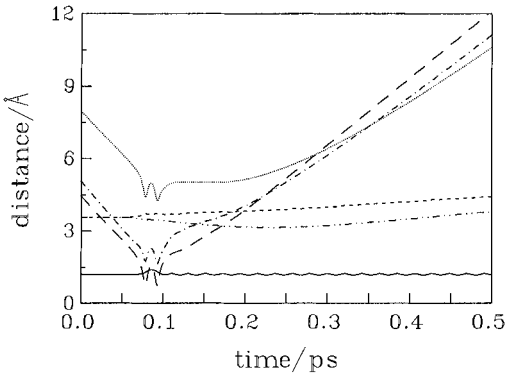

Figure 6. Distance vs time plot for a typical trajectory of the reaction H + ArO_2 → O_2 + H + Ar. The trajectory corresponds to a relative translational energy of 2.0 kcal mol^{-1}. Lines are as in Figure 4.

time. This suggests the existence of a dynamical bottleneck for the energy randomization among the HO_2 degrees of freedom. Additionally, Figures 4 and 5a seem to indicate that the formation of HO_2 products occurs through indirect-type collisions.

Unlike formation of HO_2, collisions leading to Ar + H + O_2 are usually of direct-type as shown in Figure 6 through a typical bond−distance plot. In fact, the collision lasts only the time required by the argon atom to leave the reaction shell, since the energy transferred from the incoming H atom is sufficient to immediately break down the two weak Ar−O bonds. It is also seen from the trajectory of Figure 6 that only a very small amount of the initial translational energy is transferred to the vibration of the O_2 product molecule; note, from the previous figures and the following, that there is initially no vibrational−rotational motion associated with the Ar−O and O−O bonds,

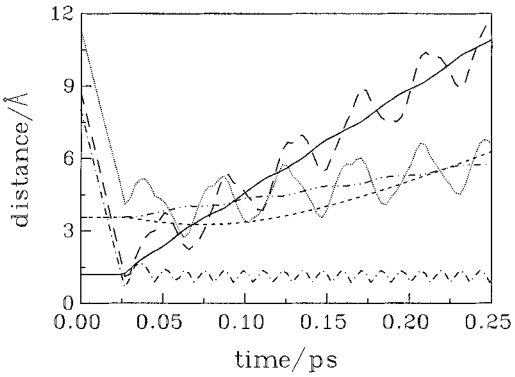

Figure 7. Distance vs time plot for a typical trajectory of the reaction H + ArO_2 → OH + O + Ar. The trajectory corresponds to a relative translational energy of 19.1 kcal mol^{-1}. Lines are as in Figure 4.

since the ArO_2 molecule has been fixed at its equilibrium geometry. Besides the nonreactive trajectories and those leading to Ar + HO_2 and Ar + H + O_2 products, only one has been found that produces O_2 + ArH (channel 11) for E_{tr} = 4.0 kcal mol^{-1} (see Table 2).

Table 3 shows the more significant results for the high range of translational energies studied in the present work. The main difference is the formation of OH molecules (or OH-type products, *i.e.*, ArOH) that arise in channels 3, 4, 6, 7, 12, and 13 (see section 5.2 for further discussion). In turn, we illustrate in Figure 7 one such trajectory that leads to formation of OH (channel 4). It is important to note from this figure the small collision time (direct-type) when compared with those leading to HO_2 at low translational energies. Although slightly longer than for Ar + H + O_2 formation (Figure 6), all energy transfer now occurs during a short period of time, which is consistent with the direct-type behavior expected for the dynamics of the title reaction at high energies. It is also clear from Figure 7 that part of the initial translational energy of the incoming hydrogen atom is retained in the vibration and rotation of OH, the remaining part being transferred to translation of the leaving argon and oxygen atoms.

4.2. Opacity Functions. Plots of the opacity function (*i.e.*, reaction probability as a function of the impact parameter) are a common way to analyze the dynamical behavior of a given collisional system. For atom + diatom systems the three atoms specify the plane where the collision takes place, and the reaction occurs in a circle centered at the diatomic center-of-mass and radius defined by the maximum impact parameter (b_{max}). For atom + triatom systems, the collision no longer occurs in a plane, while the nonzero reaction probability is now confined to a sphere with radius equal to the value of b_{max}. Thus, we need some caution to deduce dynamical features for atom + triatom systems from the corresponding opacity functions because the atoms of the reactant molecule are usually not symmetrically distributed around the corresponding center-of-mass. However, since in the present study the ArO_2 molecule has been fixed at the respective equilibrium geometry, we do not expect a great efficiency for out-of-plane collisions, especially for those energies for which the short collision times do not allow energy randomization (*i.e.*, momentum transfer). Because of this, we believe that it is reasonable to explain the opacity functions based only on the features of the potential energy surface that arise when hydrogen approaches ArO_2 in the plane (Figure 2). In such an analysis it is important to keep in mind that the dynamics of the title reaction is governed mainly by two features of the potential energy surface (see also section 2): one is related to the strong repulsion region around the Ar atom and the other is essentially due to the attractive wells of the HO_2 potential energy surface.

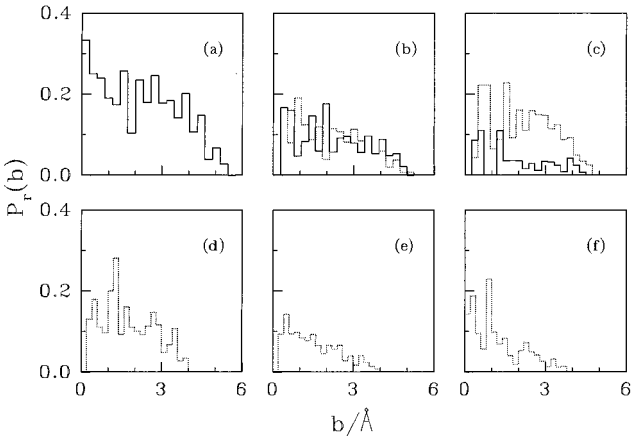

Figure 8. Opacity function for HO_2 formation at the translational energies (in kcal mol^{-1}): (a) E_{tr} = 0.25; (b) E_{tr} = 0.5; (c) E_{tr} = 1.0; (d) E_{tr} = 4.0; (e) E_{tr} = 15.5; (f) E_{tr} = 19.1. The solid lines are for formation of a stable HO_2 molecule, while the dotted ones refer to energized HO_2* species. For both E_{tr} = 0.25 and 4.0 kcal mol^{-1} only one curve is shown, since the corresponding number of trajectories is too small to be significant. See text.

In Figure 8 we present the opacity functions for HO_2 formation. Note that we have distinguished in this figure the opacity functions for HO_2 and HO_2* formation by using the solid and dotted lines, respectively. Since the HO_2 species arise only for very low translational energies, we conclude that the formation of these molecules is dictated by a capture-type mechanism where the long-range forces develop an important role as it has been found for H + O_2[49] and O + OH[49,53,56] reactions. In fact, for E_{tr} = 0.25 kcal mol^{-1} (Figure 8a), although decreasing as the orbital angular momentum increases (*i.e.*, as *b* increases), the opacity function shows approximately constant values for most of the impact parameters below b_{max}. Because of the low value of the translational energy, this can be partly transferred to the leaving Ar atom through the formation of a long-lived collision complex (see Figure 4). Thus, almost all the HO_2 molecules arise with less internal energy than the threshold for dissociation to give H + O_2 products. This assumption gives support to our recent[24] use of a chaperon mechanism to calculate the rate constant for the three-body reaction H + Ar + O_2 → HO_2 + Ar. As the initial translational energy increases, the probability of forming HO_2* complexes also increases, and for E_{tr} ≥ 4.0 kcal mol^{-1} we hardly observe formation of stable HO_2 molecules [see panels d−f in Figure 8]. Another important feature, though not explicitly shown in Figure 8, is the decreasing behavior of the opacity function for the total (stable plus energized) HO_2 formation as the translational energy increases, which appears to be due to a less significant role of long-range capture effects. In this case, the trajectories leading to HO_2 tend on average to have a more direct-type behavior.

Panels a−f of Figure 9 show the opacity functions for the reaction H + ArO_2 → O_2 + H + Ar at E_{tr} = 4.0, 8.0, 19.1, 59.3, 95.6, and 131.4 kcal mol^{-1}, respectively. It is clear from Figure 9 that the reaction probability deacreases with increasing value of the impact parameter, especially for high translational energies [panels b−f]. Obviously, the formation of Ar + H + O_2 products implies that the collision between the incoming H atom and the ArO_2 molecule would be efficient to remove the argon atom, the hydrogen atom also leaving the reaction shell. For high translational energies, this appears to be favored for head-on collisions with argon (leading to short time encounters), which are generally associated with small impact parameters,

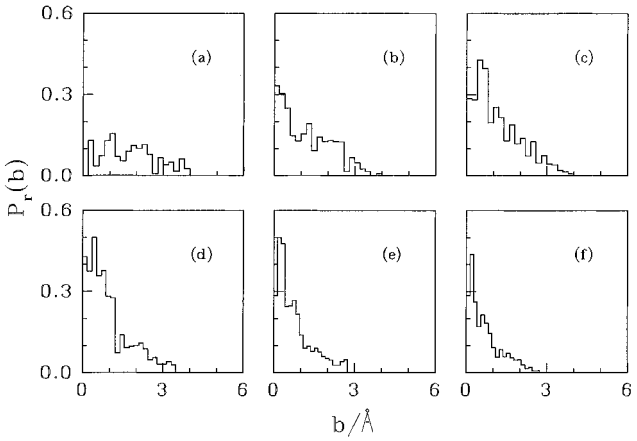

Figure 9. Opacity function for O_2 formation at the translational energies (in kcal mol^{-1}): (a) $E_{tr} = 4.0$; (b) $E_{tr} = 8.0$; (c) $E_{tr} = 19.1$; (d) $E_{tr} = 59.3$; (e) $E_{tr} = 95.6$; (f) $E_{tr} = 131.4$. See text.

since the center-of-mass of the triatomic ArO_2 molecule is close to that of the Ar atom. However, "perfect" head-on collisions with argon only occur for impact parameters different from zero, which explains the maximum of the opacity functions for $b \neq 0$ [panels c−f in Figure 9]. Moreover, we observe for $E_{tr} =$ 59.3, 95.6, and 131.4 kcal mol^{-1} [panels d−f in Figure 9] that the optimal impact parameters for O_2 formation stay around the maximum probability from $b = 0$ to $b = 1.5$ Å, while for larger values of b the opacity function suddenly decreases. This may be rationalized as follows. From Figure 2 we observe that values of $b < 1.5$ Å increase the chance for head-on collisions with argon, which favors the formation of O_2, while values of $b > 1.5$ Å enhance the probability for the approaching H atom to pass in the region of strong influence of the HO_2 deep wells, which allows for the possibility of forming other products (*e.g.*, OH molecules). Finally, as the impact parameter increases, the orbital angular momentum also increases and the opacity function tends slowly to zero. The exception to the general trend observed for the high-energy regime arises for $E_{tr} = 4.0$ kcal mol^{-1} [Figure 9a], where the opacity function presents small values for all impact parameters with a broad, small maximum around $b = 1$ Å. Indeed, as the translational energy becomes lower, the efficiency of head-on collisions with the heavy Ar atom decreases and the reaction probability (to form O_2) naturally tends to zero. For very low translational energies the O_2 molecule can hardly be formed; even if the Ar atom is allowed to leave the collision shell, the attacking H atom is promptly "captured" to form the HO_2 species. Accordingly, Table 2 shows that the O_2 formation diminishes (while the HO_2 formation increases) as translational energy decreases (see section 5.1 for further discussion on this topic).

In Figure 10 we show the opacity function for OH formation, which is an important outcome of the title reaction for translational energies above ∼13.5 kcal mol^{-1} (see Figure 3; for further discussion see section 5.2). The opacity functions presented in panels a−d of Figure 10 are for translational energies of $E_{tr} =$ 59.3, 71.7, 95.6, and 107.5 kcal mol^{-1}, respectively. Unlike the opacity function obtained by one of the authors[50] for the gas-phase reaction H + O_2 → OH + O, which shows a maximum for $b = 0$ Å and then deacreases for larger impact parameters, the curve for OH formation from the H + ArO_2 system shows the maximum probability for $b \approx 1.5$ Å. Clearly, this maximum value of the opacity function corresponds to collisions where the H atom has the opportunity to pass in the region of the HO_2 wells, which is the most efficient way to approach the O atoms. This favors the energy transfer from the incoming H atom to the outgoing O atom. Note that

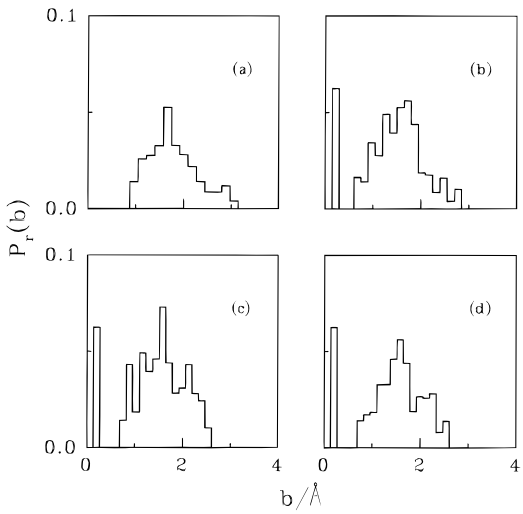

Figure 10. Opacity function for OH formation at the translational energies (in kcal mol^{-1}): (a) $E_{tr} = 59.3$; (b) $E_{tr} = 71.7$; (c) $E_{tr} = 95.6$; (d) $E_{tr} = 117.6$. See text.

argon is easily removed from the system, since it only solvates the O_2 molecule. For $E_{tr} = 59.3$ kcal mol^{-1}, the opacity function is always zero for values of b less than ∼0.9 Å. Indeed, for small impact parameters the light H atom collides directly with the Ar atom and, since the translational energy is not sufficient to avoid reflection of the incoming atom and form Ar + H + O_2, the reaction probability becomes approximately zero for low translational energies (even for those not shown in Figure 10). However, as the translational energy increases [see panels b−d of Figure 10], the approaching H atom may get deflected from the Ar atom to the attractive wells close to the O atoms, which produces the maximum in the opacity function for small impact parameters at $E_{tr} =$ 71.7, 95.4, and 107.5 kcal mol^{-1}. Note also that, for all translational energies, the opacity function is not a symmetric curve around the maximum. The enhancement of the probability of OH formation for impact parameters smaller than ∼1.5 Å may be caused by the aforementioned deflection (and a certain damping effect) of the incoming H atom, which is guided to a favorable approaching angle, allowing a more efficient collision.

Finally, we note that in general the shape of the opacity function for OH formation remains the same as the energy increases, unlike what happens for the other products just considered. Thus, we believe that OH formation depends to a large extent on steric effects.

5. Reactive Cross Sections

5.1. O_2 and HO_2 Formation. On the basis of the trajectory results of Table 2 and using eq 6, we are able to calculate the cross sections for the various channels arising in the H + ArO_2 collisions; the corresponding 68% error intervals are also obtained from eq 7. Thus, we show in Figure 11 [panel a] the reactive cross sections for HO_2 formation (excluding the energized hydroperoxyl radicals that will be treated in section 6) and the corresponding ones for H + Ar + O_2 products. The cross sections for HO_2 formation show a markedly decreasing trend with increasing translational energy. At low energies, this behavior is similar to that found in capture-dependent processes like the reaction O + OH → O_2 + H.[49,53,56] However, as the translational energy increases, the cross sections approach zero more rapidly, owing to the antithreshold energy above which no stabilized triatomic HO_2 can be formed.[24] To describe this dependence with the translational energy, we have adopted the excitation function[57]

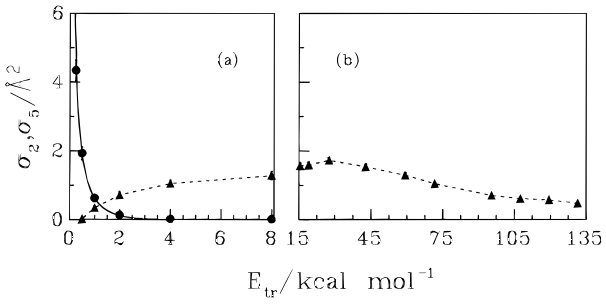

Figure 11. Cross sections as a function of translational energy for the title reaction. The cross sections for HO_2 formation (●) are significant only in the range of translational energies $0.25 \leq E_{tr}/\text{kcal mol}^{-1} \leq 8.0$. For clarity, the calculated points for channel 5 (▲) are connected with dashes. The solid line in panel a corresponds to the fit of the HO_2 formation cross sections to eq 9. The 68% confidence intervals are also shown.

$$\sigma_2(E_{tr}) = CE_{tr}^{\ n} \exp(-mE_{tr}) \tag{9}$$

where $C = 1.97$ Å^2 (kcal mol^{-1})$^{-n}$, $n = -0.77$, and $m = 1.12$ kcal^{-1} mol are adjustable parameters obtained from a least-squares fit to the calculated cross sections. Figure 11a shows that the fitted curve describes rigorously all the calculated points. For translational energies higher than 8.0 kcal mol^{-1} we do not observe formation of stable HO_2 molecules, and hence, the cross section for channel 2 vanishes.

Also shown in Figure 11 [panels a and b] are the cross sections for O_2 formation over a wide range of translational energies; the calculated points have been connected by straight dashed lines. Clearly, the cross section for O_2 formation first increases from the threshold energy at about 0.5 kcal mol^{-1} until it reaches a maximum at about $E_{tr} = 27.6$ kcal mol^{-1} and then decreases for high translational energies. Note that the small threshold for reaction H + ArO_2 → O_2 + H + Ar arises because it is a slightly endoergic process. In fact, a somewhat similar behavior is found for the endoergic reaction that leads to OH formation (see section 5.2). Thus, although the reactive cross sections for HO_2 formation are essentially capture-dependent (which corresponds to large values of σ_2 for very low translational energies), those for direct O_2 formation result mainly from head-on collisions with argon. Because of this, the calculated σ_5 never assumes large values. Finally, since O_2 formation increases as HO_2 formation decreases, and particularly σ_2 increases drastically as E_{tr} aproaches zero [note that n is negative in eq 9] while σ_5 vanishes, these two channels may be viewed as competitive for the low-energy regime [Figure 11a]. Of course, for the high energies [Figure 11b] where stabilized HO_2 molecules can hardly be formed, channel 5 competes with those leading to the formation of OH.

5.2. OH Formation. The present work makes it possible to establish the dynamical similarities (and differences) between the H + O_2 reaction and the solvated H + ArO_2 system, especially in what concerns the OH formation. Since this contains the former reaction, we are led to believe that it is possible to reproduce the cross sections for the reactive process H + O_2 → OH + O calculated using quasiclassical trajectory methods through the addition of reactive events leading to products that contain OH. For this purpose we have run trajectories for the H +ArO_2 system at translational energies $E_{tr} = 15.5$, 19.1, 27.6, 42.8, 59.3, 71.7, 95.6, 107.6, 119.5, and 131.4 kcal mol^{-1}, the first value being below the experimental H + O_2 reaction endothermicity (*i.e.*, $\Delta H = 16.6$ kcal mol^{-1}). The main results are collected in Table 3. Since the energies associated with Ar−O and Ar−H bonds are very low and the considered translational energies are high, we assume that the

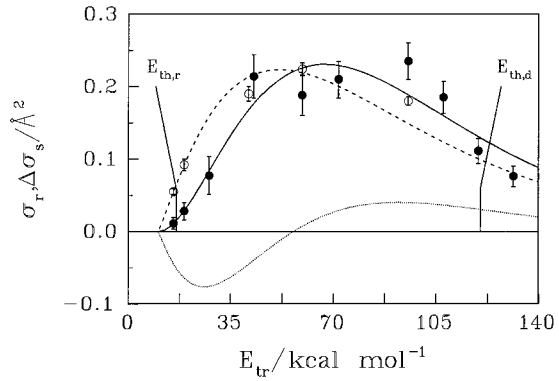

Figure 12. Cross sections for OH formation as a function of the translational energy: (● and —) this work; (○ and - - -) QCT results (ref 50); (···) $\Delta\sigma_s$ (difference between the solid and dashed lines). The lines for σ_r represent the least-squares fit to eqs 10 and 11, while the points indicate the calculated cross sections. The error bars and the threshold energies for reaction ($E_{th,r}$) and dissociation ($E_{th,d}$) are also shown.

formed ArOH molecules will dissociate at some stage to produce the Ar + OH products. Thus, we have also included the trajectories leading to O + ArOH products in the calculation of the cross sections for OH formation represented in Table 3.

Figure 12 shows the calculated cross sections for OH formation as a function of translational energy. The points shown by the black dots have been calculated by running trajectories for the title reaction, while the open ones represent the reactive cross sections for the reaction H + O_2 → OH +O obtained in ref 50 using the traditional QCT method. (It should be stressed at this point that, since we have fixed the reactant ArO_2 molecule in its equilibrium geometry, zero-point energy effects are disregarded in the present work.) We also show in Figure 12 the least-squares fit of the calculated cross sections of the form[57]

$$\sigma^{OH} = C(E_{tr} - E_{th,r})^n \exp[-m(E_{tr} - E_{th,r})] \quad (E_{tr} \geq E_{th,r}) \tag{10}$$

and

$$\sigma^{OH} = 0 \quad (E_{tr} < E_{th,r}) \tag{11}$$

where $E_{th,r}$ is the threshold energy for reaction obtained by trial and error for the QCT results (see ref 50). For comparison purposes, we have used in the present work the same value ($E_{th,r} = 10.16$ kcal mol^{-1}) for the threshold energy and have given a weight of 10 to the two cross sections closest to $E_{th,r}$ in the least-squares fit (see ref 50 for details about the QCT fit). Thus, for the parameters C, m, and n of eq 10 the numerical values arising in that least-squares fit (full curve in Figure 12) are 3.92×10^{-4} Å^2 (kcal mol^{-1})$^{-n}$ and 2.0984 and 3.695×10^{-2} kcal^{-1} mol, respectively. Although not all calculated cross sections were reproduced within the stated error bars, the two excitation functions appear to resemble the general behavior of the corresponding points. Thus, Figure 12 shows that the excitation function obtained in the present work (solid line) has the maximum slightly shifted to higher translational energies when compared to that of the corresponding curve for the nonsolvated H + O_2 calculations. Accordingly, we also show in Figure 12 the line that represents the difference between the two excitation functions, $\Delta\sigma_s = \sigma_r^{H+ArO_2} - \sigma_r^{H+O_2}$, which accounts for the solvation effects by the Ar atom. We observe that for low energies the $\Delta\sigma_s(E_{tr})$ curve assumes negative values, which seems to be due to the steric restraint of the large Ar atom as the hydrogen approaches O_2. As the translational energy

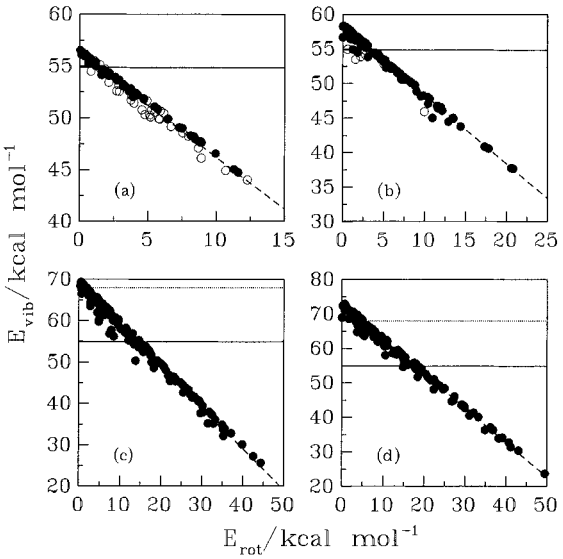

Figure 13. Vibrational−rotational energy distribution of the HO_2* complexes. Panel a refers to the initial translational energy of 2.0 kcal mol^{-1}, while panels b, c, and d correspond to 4.0, 15.5, and 19.1 kcal mol^{-1}, respectively. In each case, the solid lines indicate the vibrational threshold for the H + O_2 dissociation, while the dotted ones refer to the O + OH limit. The solid dots indicate dissociative trajectories, while the open ones correspond to HO_2* species living longer than 60 ps. Also shown in dashes is a line for constant $E_{vib} + E_{rot}$.

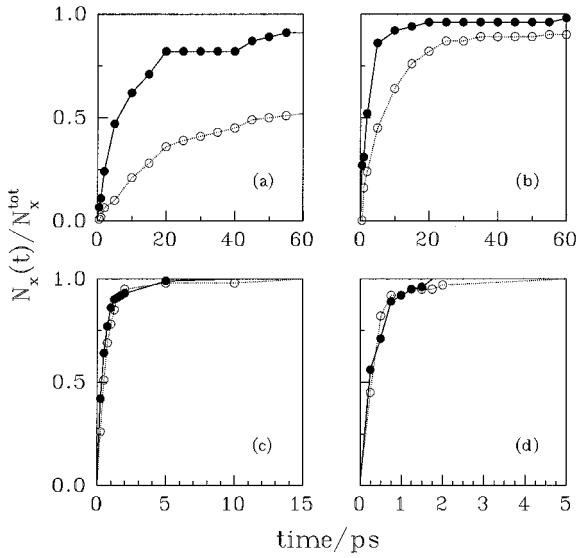

Figure 14. Fraction of dissociative HO_2* complexes with $E_{vib} \geq 54.863$ kcal mol^{-1} (−) and $E_{vib} < 54.863$ kcal mol^{-1} (···) as a function of time. Panels are as in Figure 13. See text.

increases, the argon atom no longer resists the strong hydrogen impact and acts as a damping factor during the collision, allowing a reorientation of the trajectory followed by the incoming H atom. Obviously, this effect causes an additional increase in reactivity. Note also that the dissociative cross section for $E_{tr} = 131.4$ kcal mol^{-1} is 0.008 Å^2 (only 3 trajectories lead to dissociation in 3000), while for QCT the corresponding value is 0.044 Å^2 (see Table 3). This discrepancy in the dissociative cross sections for values of E_{tr} clearly above the threshold for dissociation ($E_{th,d}$) can be understood by assuming that a large amount of the initial translational energy is transferred to the leaving Ar atom in the H + ArO_2 collisions. Typically, for high values of the translational energy, the solvation assumes little importance, since the energy is sufficient to remove the Ar atom, and the two curves tend to coalesce.

6. HO_2* Complexes after Collision

In this section we address the dynamics of the HO_2* complexes, which carry an internal energy above the threshold for H + O_2 dissociation. Thus, once a HO_2* complex has been formed, we continue the trajectory until it dissociates or the integration time reaches 60 ps, which may be considered a very long time in comparison to that required for the formation process H + $ArO_2 \rightarrow HO_2$ + Ar (typically, <1 ps). One such trajectory for initial translational energy $E_{tr} = 4.0$ kcal mol^{-1} has already been illustrated in Figure 5.

In panels a−d of Figure 13 we present the vibrational−rotational energy distribution of the HO_2* species for the initial translational energies of $E_{tr} = 2.0$, 4.0, 15.5, and 19.1 kcal mol^{-1}, respectively. From this figure, we conclude that the internal energy (E_{int}) of the HO_2* complexes is almost constant in all cases, being higher for $E_{tr} = 19.120$ kcal mol^{-1} [panel d, for which the intersect is at $E_{vib} = E_{int} \approx 72$ kcal mol^{-1}], then decreasing for $E_{tr} = 15.5$, 4.0, and 2.0 kcal mol^{-1} (for the latter $E_{vib} = E_{int} \approx 58$ kcal mol^{-1}). Thus, for each H + ArO_2 translational energy, it is possible to assign a very narrow range of HO_2 internal energies. It is apparent for $E_{tr} = 2.0$ [Figure 13a] and 4.0 kcal mol^{-1} [Figure 13b] that the points corresponding to complexes that last longer than 60 ps are the most scattered. Although some scattering is also observed for $E_{tr} = 15.5$ kcal mol^{-1} [Figure 13c], all HO_2* species dissociate to form H + O_2 products before ∼12 ps. In turn, for $E_{tr} = 19.1$ kcal mol^{-1}, the last HO_2* complex dissociates before ∼5 ps. Moreover, for this initial translational energy only three HO_2* complexes dissociate to form OH molecules, all others leading to O_2. (Although not shown, we notice that for $E_{tr} = 27.6$ kcal mol^{-1} the whole set of HO_2* complexes dissociates, but only two form OH products.) This may be due to the fact that the incoming atom is hydrogen, and hence, it is expected that the H−O_2 mode will contain most of the HO_2 vibrational energy. As a result, the formation of OH molecules after dissociation is possible only through the rapid flux of energy to the O−O stretch mode (associated with the reaction coordinate). However, we expect a weak coupling between the O−O stretch and H−O_2 bend modes (note that a similar finding has been reported[32] for the $HO_2 \rightarrow O_2$ + H reaction using quantum and semiclassical variational transition state models), which explains the formation of O_2 rather than OH.

Moreover, we indicate in Figure 13 [panels a−d] the energy threshold for H + O_2 dissociation (solid lines), while the corresponding value for forming O + OH products is shown for $E_{tr} = 15.5$ [panel c] and 19.1 kcal mol^{-1} [panel d] by the dotted lines. In turn, Figure 14 shows the time evolution of the dissociated fraction of HO_2* complexes with initial vibrational energy (E_{vib}) above and below the H + O_2 dissociation threshold (*i.e.*, 54.86 kcal mol^{-1}) for $E_{tr} = 2.0$, 4.0, 15.5, and 19.1 kcal mol^{-1} [panels a−d, respectively]. Note that the solid line ($E_{vib} \geq 54.84$ kcal mol^{-1}) is associated with the vibrational excitation while the dashed one ($E_{vib} < 54.84$ kcal mol^{-1}) accounts in a certain way for the significant rotational motion of the HO_2* complexes. From a glance at Figure 14, we immediatly observe for $E_{tr} = 2.0$ kcal mol^{-1} [panel a] an enormous increase of the HO_2* dissociative fraction for $E_{vib} \geq 54.86$ kcal mol^{-1} at lower integration times. The curve then reaches a plateau at about 20 ps, which extends up to 40 ps, and slowly increases again. For those HO_2* with $E_{vib} < 54.86$ kcal mol^{-1} the dissociative fraction always increases but more slowly than for the vibrational excitation case, the values being very separated in magnitude. However, as the translational energy increases, the two curves coalesce [panels b−d]. This appears to indicate that for high translational energies the

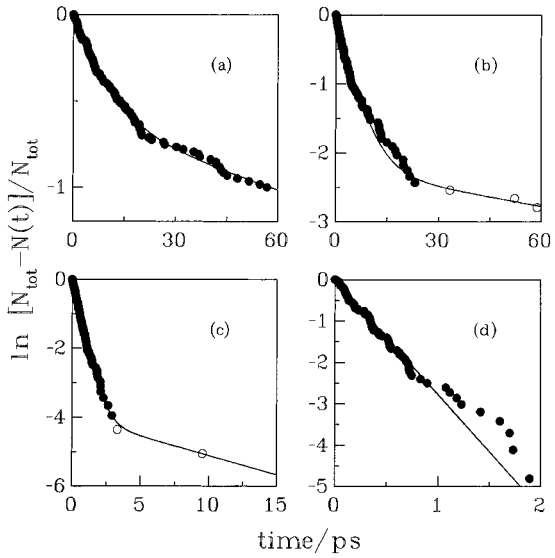

Figure 15. Logarithm of the decay rate of the HO_2* complexes as a function of time. Panels are as in Figure 13. The lines represent the least-squares fit to eqs 14 and 15, respectively, for panels a−c and panel d. In panels b and c two sets of points have been marked corresponding to distinct decay regimes. See text.

influence of rotation becomes negligible. Note also from panels a and b that a fraction of the HO_2* complexes have not been dissociated at 60 ps, that fraction being higher for those with $E_{vib} < 54.86$ kcal mol^{-1}. These observations clearly show that for most cases there is a small coupling between rotational and vibrational degrees of freedom so that the complexes need an induction time prior to dissociation, probably to allow the energy transfer into vibration associated with the dissociative H−O_2 stretching. This finding is quite consistent with the existence of "vague tori",[37] which delays the energy flow among the various degrees of freedom of the HO_2* complexes. This argument has been pointed out by Dobbyn *et al.*[33] to explain the appearance of highly excited regular states in the HO_2 energy spectrum.

Additionally, in Figure 15 we represent the logarithm of the decay rate of the HO_2* complexes as a function of time. The distribution of complex lifetimes found in Figure 15 seems to indicate that HO_2* decays with an intrinsically non-RRKM behavior,[58,59,60] especially for low energies. This situation arises, as it is well-known, when transitions between two or more individual molecular degrees of freedom are slower than transitions leading to fragments, creating one or more dynamical bottlenecks.

The mechanism leading to dissociation can then be expressed as

$$A \xrightarrow{k_a} B \xrightarrow{k_b} C \qquad (12)$$

with the thermal rate coefficients $k_a < k_b$ (or $k_a \ll k_b$). A and B stand for HO_2* complexes not coupled and strongly coupled with the reaction path, respectively, and C represents the fragments. Thus, the total fraction of HO_2* complexes present at each instant as a function of time is given by

$$f(t) = f_A + f_B = \left(f_B^0 - \frac{k_a f_A^0}{k_b - k_a}\right) \exp(-k_b t) + \left(\frac{k_a f_A^0}{k_b - k_a} + f_A^0\right) \exp(-k_a t) \qquad (13)$$

where f_A and f_B denote the fractions of A and B, with values f_A^0 and f_B^0 for $t = 0$.

TABLE 4: Relative Collision Energies, Values of Parameters k_a, k_b, f_A^0, and f_B^0 in eq 13, and Corresponding Average Lifetime of HO_2* Complexes[a]

E_{tr}/kcal mol^{-1}	k_a/ps^{-1}	k_b/ps^{-1}	f_A^0	f_B^0	$\langle\tau\rangle$/ps	$\langle\tau_{60}^{traj}\rangle$/ps	$\langle\tau_{60}^{fit}\rangle$/ps
2.0	6.79 (−3)	1.11 (−1)	0.51	0.49	84.2	14.3	14.4
4.0	9.06 (−3)	2.09 (−1)	0.10	0.90	16.2	6.1	5.9
15.5	1.39 (−1)	1.82	0.02	0.98	0.70	0.70	0.70
19.1		2.76		1.00	0.36	0.39	0.36

[a] The last two columns contain the trajectory results for the same average lifetime and the corresponding least-squares values based on eq 16.

Assuming mechanism 12, the distributions displayed in Figure 15 can then be fitted through the simple three-parameter function

$$f(t) = c_1 \exp(-c_2 t) + (1 - c_1) \exp(-c_3 t) \qquad (14)$$

which allows us to assign values to the initial fractions and average lifetimes of the individual species, as well as to estimate the overall average lifetime of the HO_2* complexes. In turn, the distribution of Figure 15d seems to exhibit an essentially RRKM-type behavior, which we describe by

$$f'(t) = f_B^0 \exp(-k_b t) \qquad (15)$$

The fitting procedure aimed to reproduce the key features of each curve, with the points being weighted with the value of the corresponding ordinate. For $E_{tr} = 2.0$ kcal mol^{-1} and $E_{tr} = 19.1$ kcal mol^{-1} direct fits to expressions 14 and 15, respectively, have been performed. For the remaining translational energies the fits have been done in two steps, one for each decay regime. The points used in each step are marked with different symbols in Figure 15.

Table 4 displays the initial fraction of A and B, the decaying constants for each species, the total average lifetime of the HO_2* complexes, and the corresponding result based on the trajectories. The trend followed as the internal energy increases is what would be expected: the fraction of A diminishes as the fraction of B increases, the decaying constants increase, and consequently, the average lifetimes decrease. The major feature of this table is the discrepancy between the average lifetimes as extrapolated from the fitted curve and the direct trajectory results, which is absent in the case of the two higher energies. This discrepancy results from the fact that trajectories have been interrupted after 60 ps of integration, leaving 37% of nondissociated HO_2* complexes for $E_{tr} = 2.0$ kcal mol^{-1} and 5.7% for 4.0 kcal mol^{-1} (both values being closely predictable from the fitting results). If we then compute the average lifetime for the fraction that has dissociated up to 60 ps, which constitutes the only part contemplated in the trajectories,

$$\langle\tau_{60}^{fit}\rangle = \frac{\int_0^{60} [f(t) - f(60)]\, dt}{1 - f(60)} \qquad (16)$$

we get a close agreement between the trajectory calculations and the least-squares results, thus verifying the consistency of the fitting procedure. The latter values are also displayed in the last column of Table 4.

7. Conclusions

We have reported a detailed dynamics study of the H + ArO_2 reaction over the range of translational energies $0.25 \le E_{tr}$/kcal mol$^{-1} \le 131.4$. The opacity function for HO_2 formation has been shown to be mainly dictated by a capture mechanism where long-range forces play the dominant role. In fact, the

cross sections for formation of stable HO_2 molecules have been shown to deacrease with increasing translational energy. In contrast, the opacity functions for the reaction $H + ArO_2 \rightarrow O_2 + H + Ar$ have been shown to have a maximum for impact parameters around zero, which indicates that head-on collisions with argon favor O_2 formation. Thus, the reactive channels for O_2 and HO_2 formation are the only competitive channels at low translational energies. In turn, for high translational energies, the O_2 and OH product channels become the competitive ones. We have also found that in comparison with the previously reported[50] cross sections for the reaction $H + O_2 \rightarrow OH + O$, those calculated for $H + ArO_2 \rightarrow OH + O + Ar$ show significant solvation effects over the complete range of translational energies considered in the present work. Finally, we have analyzed the dynamics of the energized HO_2* species arising in the reaction $H + ArO_2 \rightarrow HO_2$* $+ Ar$. At low energies, we have assumed a two-step mechanism to describe the main features of the unimolecular decay, since the corresponding decay rates differ by more than 1 order of magnitude for those energies. This is an indication of non-RRKM behavior. However, the HO_2* dissociation process is predicted to exhibit a more pronounced RRKM-type behavior with increasing energy.

Acknowledgment. This work has been carried out under the auspices of the Junta Nacional de Investigação Científica e Tecnológica (JNICT), Portugal. The financial support of programs PRAXIS XXI and FEDER is gratefully acknowledged. This project has also benefitted from an EC grant, under Contract No. CHRX-CT 94-0436.

References and Notes

(1) Kurylo, M. J. *J. Phys. Chem.* **1972**, *76*, 3518.
(2) Carleton, K. L.; Kessler, W. J.; Marinelli, W. J. *J. Phys. Chem.* **1993**, *97*, 6412.
(3) Baulch, D. L.; Drysdale, D. D.; Horne, D. G.; Lloyd, A. C. *Evaluated Kinetic Data for High-Temperature Reactions*; CRC Press: Boca Raton, FL, 1972; Vol. 1.
(4) Wong, W.; Davis, D. D. *Int. J. Chem. Kinet.* **1974**, *1*, 401.
(5) Hsu, K.-J.; Durant, J. L.; Kaufman, F. *J. Phys. Chem.* **1987**, *91*, 1895.
(6) Baulch, D. L.; Cobos, C. J.; Cox, R. A.; Esser, C.; Frank, P.; Just, Th.; Kerr, J. A.; Pilling, M. J.; Troe, J.; Walker, R. W.; Warnatz, J. *J. Phys. Chem. Ref. Data* **1992**, 21.
(7) Getzinger, R. W.; Schott, G. L. *J. Chem. Phys.* **1965**, *43*, 3237.
(8) Blair, L. S.; Getzinger, R. W. *Combust. Flame* **1970**, *14*, 5.
(9) Fenimore, C. P.; Jones, G. W. *Symp. (Int.) Combust., [Proc.] 10th* **1965**, 489.
(10) Gutman, D.; Hardwidge, E. A.; Dougherty, F. A.; Lutz, R. W. *J. Chem. Phys.* **1967**, *47*, 4400.
(11) Pirraglia, A. N.; Michael, J. V.; Sutherland, J. W.; Klemm, R. B. *J. Phys. Chem.* **1989**, *93*, 282.
(12) Clyne, M. A. A.; Thrush, B. A. *Proc. R. Soc., Ser. A* **1963**, *275*, 559.
(13) Larkin, F. S.; Thrush, B. A. *Discussions Faraday Soc.* **1964**, *37*, 112.
(14) Dodonov, A. F.; Lavrovakaya, G. K.; Talrose, V. L. *Kinet. Katal.* **1969**, *10*, 701.
(15) Biship, W. P.; Dorfman, L. M. *J. Chem. Phys.* **1970**, *52*, 3210.
(16) Hikida, T.; Eyre, J. A.; Dorfman, L. M. *J. Chem. Phys.* **1971**, *54*, 3422.
(17) Westenberg, A. A.; de Haas, N. *J. Phys. Chem.* **1972**, *76*, 1586.
(18) Moortgat, G. K.; Allen, E. R. 163rd National Meeting of the American Chemical Society, Boston, 1972.
(19) Galluci, C. R.; Schatz, G. C. *J. Phys. Chem.* **1982**, *86*, 2352.
(20) Brown, N. J.; Miller, J. A. *J. Chem. Phys.* **1984**, *80*, 5568.
(21) Melius, C. F.; Blint, R. J. *Chem. Phys. Lett.* **1979**, *64*, 183.
(22) Gelb, A. *J. Phys. Chem.* **1985**, *89*, 4189.
(23) Varandas, A. J. C.; Murrell, J. N. *Chem. Phys. Lett.* **1982**, *88*, 1.
(24) Varandas, A. J. C.; Pais, A. A. C. C.; Marques, J. M. C.; Wang, W. *Chem. Phys. Lett.* **1996**, *249*, 264.
(25) Gross, A.; Billing, G. D. *Chem. Phys.* **1993**, *173*, 393.
(26) Rabinowitch, E. *Trans. Faraday Soc.* **1937**, *33*, 283.
(27) Bunker, D. L. *J. Chem. Phys.* **1960**, *32*, 1001.
(28) Benson, S. W.; Fueno, T. *J. Chem. Phys.* **1962**, *36*, 1597.
(29) Sheppard, M. G.; Walker, R. B. *J. Chem. Phys.* **1983**, *78*, 7191.
(30) Yamashita, K.; Morokuma, K.; Le Queré, F.; Leforestier, C. *Chem. Phys. Lett.* **1992**, *191*, 515.
(31) Murrell, J. N.; Carter, S.; Farantos, S. C.; Huxley, P.; Varandas, A. J. C. *Molecular Potential Energy Functions*; Wiley: Chichester, 1984.
(32) Song, K.; Peslherbe, G. H.; Hase, W. L. *J. Chem. Phys.* **1995**, *103*, 8891.
(33) Dobbyn, A. J.; Stumpf, M.; Keller, H.-M.; Schinke, R. *J. Chem. Phys.* **1995**, *103*, 9947.
(34) Mandelshtam, V. A.; Grozdanov, T. P.; Taylor, H. S. *J. Chem. Phys.* **1995**, *103*, 10074.
(35) Pastrana, M. R.; Quintales, L. A. M.; Brandão, J.; Varandas, A. J. C. *J. Phys. Chem.* **1990**, *94*, 8073.
(36) Varandas, A. J. C.; Bowman, J. M.; Gazdy, B. *Chem. Phys. Lett.* **1995**, *233*, 405.
(37) Shirts, R. B.; Reinhardt, W. P. *J. Chem. Phys.* **1982**, *77*, 5204.
(38) Davis, M. J. *J. Phys. Chem.* **1988**, *92*, 3124.
(39) Dai, J.; Zhang, J. Z. H. *J. Phys. Chem.* **1996**, *104*, 3664.
(40) Varandas, A. J. C.; Silva, J. D. *J. Chem. Soc., Faraday Trans. 2* **1986**, *82*, 593.
(41) Aquilanti, V.; Liuti, G.; Pirani, F.; Vecchiocattivi, F.; Volpi, G. G. *J. Chem. Phys.* **1976**, *65*, 4751.
(42) Este, G. O.; Knight, D. G.; Scoles, G.; Valbusa, U.; Grein, F. *J. Phys. Chem.* **1983**, *87*, 2772.
(43) Raff, L. M. *J. Chem. Phys.* **1966**, *44*, 1202.
(44) Raff, L. M.; Thompson, D. L.; Sims, L. B.; Porter, R. N. *J. Chem. Phys.* **1972**, *56*, 5998.
(45) Porter, R. N.; Karplus, M. *J. Chem. Phys.* **1964**, *40*, 1105.
(46) Karplus, M.; Porter, R. N.; Sharma, R. D. *J. Chem. Phys.* **1965**, *43*, 3259.
(47) Truhlar, D. G.; Muckerman, J. T. *Atom-Molecule Collision Theory*; Bernstein, R. B., Ed.; Plenum Press: New York, 1979; p 505.
(48) Miller, J. A. *J. Chem. Phys.* **1981**, *74*, 5120.
(49) Varandas, A. J. C.; Brandão, J.; Pastrana, M. R. *J. Chem. Phys.* **1992**, *96*, 5137.
(50) Varandas, A. J. C. *J. Chem. Phys.* **1993**, *99*, 1076.
(51) Varandas, A. J. C. *Chem. Phys. Lett.* **1994**, *225*, 18.
(52) Varandas, A. J. C. *Chem. Phys. Lett.* **1995**, *235*, 111.
(53) Varandas, A. J. C.; Marques, J. M. C. *J. Chem. Phys.* **1992**, *97*, 4050.
(54) Varandas, A. J. C.; Marques, J. M. C. *J. Chem. Phys.* **1994**, *100*, 1908.
(55) Hase, W. L. Mercury: a general Monte Carlo classical trajectory computer program. *QCPE* 453.
(56) Marques, J. M. C.; Wang, W.; Varandas, A. J. C. *J. Chem. Soc., Faraday Trans.* **1994**, *90*, 2189.
(57) LeRoy, R. L. *J. Phys. Chem.* **1969**, *73*, 4338.
(58) Hase, W. L. *Acc. Chem. Res.* **1983**, *16*, 258.
(59) Marcus, R. A.; Hase, W. L.; Swamy, K. N. *J. Phys. Chem.* **1984**, *88*, 6717.
(60) Wardlaw, D. M.; Marcus, R. A. *Adv. Chem. Phys.* **1988**, *70*, 231.

JP961863A